

Persistence behavior in African trypanosomes during adipose tissue colonization

Sandra Trindade

Instituto de Medicina Molecular, Faculdade de Medicina, Universidade de Lisboa

Mariana De Niz

Instituto de Medicina Molecular, Faculdade de Medicina, Universidade de Lisboa

Mariana Sequeira

Instituto de Medicina Molecular, Faculdade de Medicina, Universidade de Lisboa

<https://orcid.org/0000-0003-1486-5403>

Tiago Bizarra-Rebello

Instituto de Medicina Molecular, Faculdade de Medicina, Universidade de Lisboa

Fabio Bento

Instituto de Medicina Molecular, Faculdade de Medicina, Universidade de Lisboa

Mario Dejung

Institute of Molecular Biology

Joao Ferreira

Instituto de Medicina Molecular, Faculdade de Medicina, Universidade de Lisboa

Falk Butter

Institute of Molecular Biology

Frederic Bringaud

University of Bordeaux

Erida Gjini

Instituto Gulbenkian de Ciência

Luisa Figueiredo (✉ lmf@medicina.ulisboa.pt)

Instituto de Medicina Molecular, Faculdade de Medicina, Universidade de Lisboa

<https://orcid.org/0000-0002-5752-6586>

Article

Keywords: Trypanosoma brucei, persistence, sleeping sickness

Posted Date: May 20th, 2021

DOI: <https://doi.org/10.21203/rs.3.rs-499897/v1>

License:  This work is licensed under a Creative Commons Attribution 4.0 International License.

[Read Full License](#)

Persistence behavior in African trypanosomes during adipose tissue colonization

Sandra Trindade¹, Mariana De Niz¹, Mariana Costa-Sequeira¹, Tiago Bizarra-Rebelo¹, Fábio Bento^{1*}, Mario Dejung², João Ferreira¹, Falk Butter², Frédéric Bringaud^{3,4}, Erida Gjini^{5*} & Luisa M. Figueiredo^{1*}.

¹Instituto de Medicina Molecular João Lobo Antunes, Faculdade de Medicina, Universidade de Lisboa, 1649-028 Lisbon, Portugal

²Institute of Molecular Biology, 55128 Mainz, Germany

³Laboratoire de Microbiologie Fondamentale et Pathogénicité (MFP), Université de Bordeaux, CNRS UMR-5234, Bordeaux, France

⁴Centre de Résonance Magnétique des Systèmes Biologiques (RMSB), Université de Bordeaux, CNRS UMR-5536, Bordeaux, France

⁵Instituto Gulbenkian de Ciência, 2780-156 Oeiras, Portugal

*Current address: Institute of Molecular Biology, Mainz, Germany

*Current address: Center for Computational and Stochastic Mathematics, Instituto Superior Técnico, Universidade de Lisboa, 1049-001 Lisbon, Portugal.

*Luisa M. Figueiredo, Erida Gjini.

Email: lmf@medicina.ulisboa.pt and erida.gjini@tecnico.ulisboa.pt

33 Abstract

34 Persistence is an important and ancient evolutionary adaptive mechanism used by several
35 organisms to survive environmental changes. During its life cycle *Trypanosoma brucei*, the
36 causative agent of sleeping sickness, inhabits several microenvironments, including the adipose
37 tissue. Here we used a mathematical model to investigate how this large parasite reservoir
38 contributes to the global parasite population dynamics. By modeling the total number of parasites
39 and the proportion of transmissible forms in the blood and the adipose tissue during an infection,
40 we estimated that adipose tissue parasites proliferate more slowly. Intravital microscopy of
41 parasites stained with CellTrace™ Violet confirmed that adipose tissue forms divide twice slower
42 than the blood counterparts. Consistent with a reduced growth, proteome analysis revealed that
43 adipose tissue forms undergo a metabolic adaptation and downregulate proteins involved in
44 translation. Quantification of protein synthesis using L-Homopropargylglycine confirmed that this
45 rate is 24% lower in adipose tissue parasites. We propose that in adipose tissue, *T. brucei* acquire
46 a persistence-like behavior, which could contribute to disease chronicity and treatment failure.

47

48

49 Persistence was first described in bacteria and has been well characterized in several
50 different bacterial species ever since¹. Persisters are a subgroup of viable cells of a population
51 characterized by growth arrest or slower growth, altered metabolism, downregulation of protein
52 synthesis and increased resistance to environmental threats such as immunological attack and
53 drug treatment. This condition is reversible and persisters can return to a more proliferative state.
54 Among parasitic protozoa, the existence of persisters has only been recently documented, and
55 knowledge on the biological roles of these parasites subpopulations is still scarce². *Toxoplasma*
56 *gondii*, a protozoan parasite that infects most species of warm-blooded animals, upon host
57 invasion, disseminate into tissues and differentiate into persistent metabolically active, slow grower
58 bradyzoites as a strategy to overcome nutrient limitations and host immune pressure³. Persistence
59 can also be triggered by temporary exposure to external stresses. *P. falciparum*, for instance,
60 spontaneously develops into dormant ring stages with a distinct metabolic state upon artemisinin
61 exposure⁴. Importantly, these persistent parasitic protozoa are refractory to artemisinin-based
62 drugs promoting drug treatment failure².

63 *Trypanosoma brucei* parasites, the causative agents of Human African Trypanosomiasis
64 (HAT), have a complex life cycle that oscillates between a tsetse vector and a mammalian host.
65 During the mammal infection, parasites invade and occupy the interstitial spaces of different
66 organs, such as the central nervous system, adipose tissue and skin⁵. Transmission between hosts
67 is ensured by the quiescent non-dividing stumpy forms and metacyclic forms. These non-replicative
68 forms are pre-adapted to survive in the tsetse midgut and the mammalian host environments,
69 respectively. Stumpy forms are also important to reduce global parasite load in the mammalian
70 host. Similar to what has been described in bacteria, these parasites change their metabolism and
71 reduce their protein synthesis^{6,7}.

72 A different source of heterogeneity within a *T. brucei* population stems from the adaptation
73 to the tissue environment. We have previously shown that, in a mouse infection, adipose tissue is
74 one of the largest reservoirs of *T. brucei* parasites^{8,9} occupied by Adipose Tissue Forms (ATFs).
75 These forms are functionally different from the bloodstream counterparts (BSFs), with a metabolism
76 apparently adapted to catabolize fatty acids and are capable of re-infecting the blood circulation,
77 showing that they are not terminally differentiated to live exclusively in the adipose tissue⁸.

78 In this work, we use mathematical modelling to determine key parameters that govern *T.*
79 *brucei* chronic infections taking into account the existence of tissue reservoirs. We experimentally
80 confirmed the prediction of the model for differences between reservoirs, showing that the adipose
81 tissue harbors slow growing parasites that synthesize proteins at a lower rate. Together with
82 previous knowledge that ATFs are metabolically distinct from the blood counterparts⁸, we propose
83 the existence of persister-like cells in the adipose tissue population. This finding has important
84 implications in our understanding of drug resistance and relapses, and reveals that adipose tissue
85 acts as a reservoir of quieter parasites that may cause less pathology and thus contribute to disease
86 chronicity.

87

88 Results

89

90 Parasite dynamics differ between blood and adipose tissue

91 Adipose tissue is a major parasite reservoir during the acute and the chronic stages of the
92 disease in mice. We previously observed that, on day 6 of infection, the adipose tissue is mainly
93 populated by slender forms, while the blood has a majority of transmissible stumpy forms⁸. Whether
94 the parasite load remains high in the adipose tissue and the proportion of slender and stumpy forms
95 varies in the two tissues, throughout infection, remains unknown. To answer this question, we
96 infected mice with a pleomorphic *GFP::PAD1_{utr}* reporter parasite line that allowed us to follow both
97 the total parasite load, and the proportion of transmissible forms (because stumpy forms are GFP-
98 expressers) in each tissue for over 28 days of infection⁸. Mice were sacrificed on 17 days of
99 infection and the total number of parasites per organ (parasite load) was quantified by qPCR from
100 genomic DNA isolated from blood and perfused gonadal adipose tissue. BSFs and ATFs were also
101 isolated from both tissues to assess the percentage of stumpy forms by flow cytometry.

102 In general, both tissues remained highly parasitized throughout infection. When we
103 compared parasite density (parasites/mg), the gonadal adipose tissue was on average ~6-fold
104 more concentrated than blood. When we compared the parasite load (number of parasites in whole
105 organ), the blood had on average ~1.4-fold more parasites than gonadal adipose tissue
106 (Supplementary Table S1). As previously observed^{8,10,11}, during the first week of infection, the blood
107 showed a larger range of parasite load with a peak in total number of parasites on day 6 (~10⁸
108 parasites) and a subsequent trough on day 8 (~2x10³ parasites). During this period, the number of
109 parasites in the gonadal adipose tissue varied less (10⁴-10⁷ parasites) (Fig. 1A and Supplementary
110 Table S1). These results showed an initial slower colonization of the adipose tissue and a less
111 pronounced reduction of this population after day 6 of infection, as revealed by the roughly 1,000-
112 fold more parasites in the gonadal adipose tissue than in the blood at days 7 and 8 post infection.
113 From day 13 forward, the total number of parasites was less variable and the pattern more similar
114 between tissues (~10⁶-10⁷ parasites), with the blood having on average around 3-fold more
115 parasites than the gonadal adipose tissue (Fig. 1A and Supplementary Table S1). Since parasite
116 load was not measured daily, we cannot discard the possible existence of other troughs, although
117 this is highly unlikely because others have shown that parasitemia remains relatively high after day
118 12 of infection¹⁰.

119 Next, we assessed if the proportion of replicative (slender) and non-replicative
120 transmissible (stumpy) forms is different between the two tissues throughout infection. Parasites
121 were isolated from blood and gonadal adipose tissue and flow cytometry was used to calculate the
122 proportion of parasites that expressed GFP (stumpy reporter gene driven by 3'UTR of PAD1)¹². In
123 general, we observed that in the adipose tissue, the average percentage of stumpy forms was
124 lower (Wilcoxon Signed Rank test, p<0.0001) and more evenly distributed than in the blood. While
125 the adipose tissue percentage of stumpy forms is normally distributed (Kolmogorov–Smirnov Test,
126 p>0.1) with a mean of 52% and a standard deviation of 31%, the blood percentage of stumpy forms
127 follows a non-normal distribution (Kolmogorov–Smirnov Test, p<0.0001) with a mean of 79% and
128 a standard deviation of 28% (Fig. 1B). Indeed, except for day 4, the blood was always richer in
129 stumpy forms than the gonadal adipose tissue. Interestingly, for the first two weeks of infection, the
130 accumulation of stumpy forms in the adipose tissue proceeds more slowly than in the blood. This
131 is consistent with the fact that in most days of the infection, the parasite load in blood is higher than
132 in adipose tissue (Fig. 1A). When we compare data from an individual mouse, it is also possible to
133 observe that the proportion of stumpy forms can be dramatically different between the two
134 microenvironments (Fig. 1C), indicating that within a single animal there are significant differences
135 in the proportion of stumpy forms across tissues.

136 We conclude that although blood and gonadal adipose tissue are highly parasitized
137 throughout infection, the dynamics of the number of parasites and the proportion of slender/stumpy
138 forms are different between the two compartments. Relative to the blood, the adipose tissue is
139 poorer in stumpy forms. These results suggest an influence from the tissue microenvironment and
140 the existence of an important barrier (likely, the vasculature) that prevents homogenization of the
141 two parasite populations.

142

143 **Infection modeling anticipates differences in parasite growth between tissues**

144 To quantify the infection processes in more detail, and investigate parameter differences
145 between microenvironments, we built a mathematical model that describes parasite growth,
146 differentiation, antigenic variation dynamics and the interplay with host immunity. The model was
147 based on a previous mathematical formulation¹³, but was now extended to include two connected
148 in-host compartments: blood and adipose tissue, with parasite migration between them (Fig. 2A
149 and Supplementary Model Information). The primary aim of the model was to integrate under the
150 same mechanistic framework the empirical data on the parasite density and the proportion of
151 stumpy forms across the two compartments over time. Parasite density was used instead of total
152 number of parasites to avoid misinterpretations derived from the observed fluctuations in the
153 adipose tissue weight (Supplementary Table S1). While some model parameters were assumed
154 fixed at biologically reasonable values (Supplementary Table S2), other key infection parameters
155 were estimated (Table 1).

156 To test for plausible parameter differences between the blood and adipose tissue, we
157 considered three nested versions of the model. In model 1 (the null hypothesis), no infection
158 parameter differences between compartments were assumed (except for the blood exclusive onset
159 of infection and antigen switching); in model 2, the parasites may grow at different rates in each
160 compartment; in model 3, in addition to growth rates, differentiation parameters could also vary
161 across the two tissues. Although the model structure is flexible enough to explore many more
162 hypotheses about parameter differences between compartments, we limited our analysis to these
163 three basic formulations, differing sequentially in just one parameter, which are the simplest ones
164 to start with, and easier to validate with additional experiments.

165 We fitted each model dynamically to the experimental data under a Bayesian framework,
166 and then compared their results based on the Deviance Information Criterion (DIC)¹⁴, the likelihood
167 ratio¹⁵, as well as the visual inspection of the 95% credible envelopes for the infection trajectories.
168 Model fits generated model-specific estimates for infection parameters and corresponding
169 predictions for the inter-coupled infection dynamics between blood and adipose tissue, even though
170 the models are realistically close to each other (Table 1 and Supplementary Model Information).
171 The DIC criterion and the likelihood ratio test were the statistical indicators that allowed comparing
172 how well the models fit the raw data, balancing quality of fit with model complexity. Typically, models
173 with a smaller DIC are favored. In addition, a large likelihood ratio would favor the more complex
174 model while a small likelihood ratio would favor the simpler model. For this specific dataset, model
175 2 was favored over model 1 by both the above criteria. The model was able to capture accurately
176 the global parasite dynamics across the blood and adipose tissue over 28 days (Fig. 2B and
177 Supplementary Model Information). Further adding an extra layer of complexity, by allowing
178 variation of the differentiation parameter across the two compartments (model 3), produced largely
179 overlapping estimates for these infection traits in blood and adipose tissue and did not significantly
180 improve the model fit (Supplementary Table S3).

181 The key parameter change between the null model 1 and favored model 2 is the difference
182 in parasite growth rates between the two compartments. While model 1 estimated a single growth
183 rate for the entire population as a null-hypothesis, model 2 estimated a doubling time of 7 hours for
184 the parasite population in the blood and 13.7 hours for parasites residing in the adipose tissue. This
185 observation is in good agreement with previous modeling where bloodstream form parasites were
186 estimated to divide every 6 hours¹⁶. The inferred 50% lower growth rate of slender forms in the
187 adipose tissue (Table 1), enabled model 2 to better describe the observed slow buildup of stumpy
188 forms over time in this tissue. This indicates that allowing for heterogeneous replication of slender
189 form parasites between the blood and adipose tissue is both necessary and sufficient to capture
190 the global patterns in the experimental infection data over 28 days (Fig. 2B and Supplementary
191 Model Information).

192 Overall, going beyond single snapshot analysis, and accounting for the inter-dependent
193 temporal structure and feedbacks between infection variables, we were able to integrate in a
194 dynamic model the experimental data on *T. brucei* parasite density and the proportion of stumpy
195 forms in blood and adipose tissue of infected mice. The best-fitting model indicates that the
196 replication of parasites residing in the adipose tissue is 2-fold slower than the ones in the blood.
197

198 **Proteome analysis suggests downregulated protein translation in ATFs**

199 To experimentally validate the model prediction that slender forms in the adipose tissue
200 grow twice longer than in the blood, we started by comparing the proteome of slender forms isolated

201 from blood and gonadal adipose tissue. Given that the proteome of stumpy and slender forms is
202 different¹⁷, and stumpy forms are present in unequal amounts in the two tissues, we chose to infect
203 mice with a monomorphic strain, which does not form stumpy forms. Five days post-infection,
204 parasites were isolated from blood and adipose tissue and processed for proteome analysis.

205 We identified a total of 2693 protein groups among ATF and BSF parasites (Supplementary
206 Dataset S1), from which 6% were differentially expressed, namely, 54 protein groups were
207 upregulated and 112 protein groups were downregulated in the ATFs (Fig. 3A). The relative
208 abundances of the differentially expressed protein groups showed high consistency between
209 replicates (Fig. 3B), suggesting that the differences detected between ATF and BSF parasites are
210 reproducible between infections in different animals.

211 To identify which processes may be downregulated in ATFs, we performed a Gene
212 Ontology (GO) term enrichment analysis of the downregulated proteins (Fisher's exact test,
213 $p \leq 0.05$). The biological process ontology showed significant depletion of two GO terms, namely,
214 translation and ribosome biogenesis (Supplementary Table S4). Among those, the most significant
215 alteration that took place in ATFs was the down-regulation of proteins involved in translation (Fig.
216 3C and Supplementary Dataset S1 and Table S4). 96 ribosomal proteins of 208 annotated protein
217 groups within this GO term were down-regulated in the ATF proteome. Ribosome biogenesis, a
218 pivotal process for protein translation was also diminished. A curated analysis of the proteins
219 revealed that multiple ribosomal proteins of both 40S and 60S ribosomal subunits were
220 downregulated. Interestingly, despite not annotated to any of the obtained GO terms, the second
221 largest subunit of the RNA polymerase I was also downregulated (Tb927.11.630, fold change of
222 0.5) suggesting a lower transcription of ribosomal gene units (Supplementary Dataset S1 and Table
223 S4). These data strongly suggest that ATFs undergo a generalized reduction in the machinery
224 responsible for synthesizing proteins.

225 GO term analysis of the proteins upregulated in ATFs (Supplementary Table S4) suggests
226 that these parasites are metabolically distinct from BSFs, which is consistent with our previous
227 transcriptomic and biochemical characterization⁸. Interestingly, the most significant category of up-
228 regulated proteins comprised purine metabolism (5 of the 54 upregulated protein groups) (Fig. 3C).
229 The upregulation of the purine nucleoside transporter, with high affinity for adenosine, and
230 adenosine transporter 2 ((Tb927.9.7470 and Tb927.2.6150, respectively, fold change 6.8), together
231 with inosine-adenosine-guanosine-nucleosidehydrolase (Tb927.3.2960, fold change 1.8) and
232 adenine phosphoribosyltransferase (Tb927.7.1780, fold change 2.0) (Fig. 3C and Supplementary,
233 Dataset S1 and Table S4), could culminate in increased cellular levels of adenosine
234 monophosphate (AMP) and consequently stimulate the ATP production and/or affect the AMP/ATP
235 ratio.

236 Mitochondrial pathways involved in central metabolism are also upregulated in ATFs with
237 evidence in the proteome of upregulated enzymatic reactions involved in ATP metabolism (13 of
238 the 54 upregulated genes). Namely, the upregulation of two of the three enzymes composing the
239 mitochondrial acetate production pathway, which is involved in ATP production in the
240 mitochondrion¹⁸⁻²⁰, i.e. the pyruvate dehydrogenase complex (PDH; Tb927.3.1790,
241 Tb927.10.12700 and Tb927.10.2350, fold change of 2.0) and acetate:succinate CoA-transferase
242 (ASCT; Tb927.11.2690, fold change of 2.7). Also, enzymes of the glutamine catabolic pathway,
243 which has been reported to be functional in BSFs²¹ and participate in ATP production, are
244 upregulated in ATFs. This includes glutamate dehydrogenase (Tb927.9.5900, fold change 2.8),
245 which converts glutamate to α -ketoglutarate and the α -ketoglutarate dehydrogenase complex
246 (Tb927.11.11680, Tb927.11.1450 and Tb927.11.9980, fold changes 1.9, 3.4 and 3.1, respectively)
247 (Supplementary Dataset S1). It is noteworthy that the proline degradation pathway, which includes
248 the upregulated delta-1-pyrroline-5-carboxylate dehydrogenase (Tb927.10.3210, fold change 1.9),
249 also produces glutamate that can then be converted into α -ketoglutarate as well. In addition, the
250 proteome of ATFs suggested a concomitant expanded use by the mitochondrial F_1/F_0 -ATP
251 synthase of the ATP produced in the mitochondrion. Indeed, the absent expression of any
252 component of the oxidative phosphorylation pathway together with the increased expression levels
253 of four mitochondrial F_1/F_0 -ATP-synthase subunits pointed towards a reverse mode of action with
254 a concomitant ATP hydrolyzation in these parasite forms. Namely, the F_1 complex subunit gamma
255 (Tb927.10.180, fold change 1.7), the F_0 complex subunit B (Tb927.5.1710, fold change of 1.8), the
256 subunit 5 (Tb927.10.8030, fold change 1.6) and the putative ATP synthase subunit (Tb927.5.3090,

257 fold change 2.3) (Supplementary Dataset S1) of the mitochondrial F₁/F₀-ATP-synthase showed
258 increased expression levels.

259 Curiously, evidence for an increased oxidative stress response was also observed in the
260 adipose tissue parasites (oxidation-reduction process group) (Fig. 3C), with the upregulation of
261 iron/ascorbate oxidoreductase family protein and iron superoxide dismutase A (Tb11.v5.0215 and
262 Tb927.5.3350, fold changes 6.3 and 1.8, respectively) (Supplementary Dataset S1), probably as
263 part of the adaptation process to the new environment.

264 In summary, the proteome analysis revealed that the slender forms that live in the adipose
265 tissue and blood present significantly different proteomes. Gene function analysis revealed that
266 ATFs have a reduced protein synthesis and a remodeled metabolism that is oriented towards
267 AMP/ATP production and increased mitochondrial activity.

268

269 **ATFs have reduced protein synthesis**

270 Next, we investigated whether the protein synthesis of adipose tissue parasites is lower
271 than in blood parasites. We measured protein synthesis by labeling newly synthesized proteins
272 with a methionine analog, Click-iT[®] Homopropargylglycine (HPG), in parasites isolated from each
273 of the two tissues. Levels of labelled nascent proteins in BSFs and ATFs were measured by flow
274 cytometry. Given that this method has never been optimized for *T. brucei*, first we tested the
275 linearity of the assay by cultivating bloodstream forms in three increasing concentrations of HPG
276 (25µg, 50µg and 100µg) for 30 minutes. The Mean Fluorescence Intensity (MFI) measured by flow
277 cytometry showed a dose-dependent response in which the levels of labelled proteins increased
278 with the levels of HPG (Supplementary Fig. S1A). In all subsequent experiments, 50µg of HPG
279 were used. Next, we compared the protein synthesis between BSFs and Procyclic Forms (PCFs).
280 Previous studies using ³⁵S-methionine-labelling, showed that the protein synthesis of PCFs is 25-
281 37% lower than BSFs²². Our HPG-labelling assay revealed that PCFs incorporated on average
282 74% less HPG than BSFs (Supplementary Fig. S1B), which is consistent although more
283 pronounced than previously reported²². Differences in the parasite strains, medium composition
284 and growth conditions may explain the observed discrepancies between the two studies. To confirm
285 that HPG intensity was a result of its incorporation into proteins and not of free HPG inside the
286 parasites, we inhibited protein synthesis of cultured parasites with cycloheximide. We observed
287 that the levels of HPG intensity dropped to 7% of condition without cycloheximide, validating our
288 assay (Supplementary Fig. S1C).

289 To compare the protein synthesis of parasites from different tissues *ex vivo*, we infected
290 mice with the same monomorphic strain that is incapable of differentiating to stumpy forms, a life
291 cycle stage that is well known to also have a reduced protein synthesis. Mice were sacrificed on
292 day 5 post-infection and parasites were isolated from blood and gonadal adipose tissue in parallel.
293 In each of the six independent experiments, parasites from 4-5 mice were pooled prior to HPG
294 labelling. After incubation for 30 minutes with HPG, parasites were washed and analyzed as
295 indicated in Fig. 3D. Flow cytometry revealed that the intensity of HPG signal was 24% lower in
296 parasites isolated from adipose tissue than from blood (Fig. 3E). Although the absolute levels of
297 HPG-labelled proteins showed some variability between independent experiments, the intensity of
298 HPG-labelled proteins was always lower in ATFs than BSFs (with a range of reduction between
299 14%-35%) (Fig. 3F), indicating that adipose tissue forms have a reduced protein synthesis
300 (Wilcoxon Signed Rank Test, p<0.05).

301

302 **Parasites in the adipose tissue proliferate more slowly than in the blood**

303 In many eukaryotes, a reduced rate of protein synthesis is normally associated to slower
304 growth^{23,24}. Our modeling analysis indeed suggested that in the adipose tissue parasites replicate
305 every 13hr42min, unlike 7hr6min in the blood (Table 1). To test whether ATFs replicate more slowly
306 than BSFs, we started by analyzing the cell cycle pattern of ATFs vs BSFs. First, we used intravital
307 imaging to compare the number of kinetoplasts/nuclei (KsNs)²⁵ in parasites present in blood and
308 adipose tissue. Intravenous administration of Hoechst to mice infected for 5 days with a
309 monomorphic strain (Fig. 4A and Supplementary Movie S1) revealed that ATFs have on average
310 a significantly higher percentage of parasites presenting 1K1N (cells in G1, early S phase or G0-
311 arrested cells) (73.6% vs 60.1% in BSFs) and 2K1N (G2 and mitotic cells) (17.1% vs 11.6% in
312 BSFs) configurations. The most significant difference was that ATFs have a lower percentage of
313 2K2N parasites (post-mitotic) (9.3% vs 28.3% in BSFs), suggesting that in a snapshot of the ATF
314 population it is less likely to find parasites that just underwent cell division than in a BSF population,

315 which would be expected if ATFs proliferate more slowly (Fig. 4B). An *ex vivo* parallel analysis on
316 parasites previously isolated from blood and adipose tissue, showed similar results, indicating that
317 *ex vivo* cell cycle analysis is a valid method for future studies (Supplementary Fig. S2A).

318 To further confirm the differences of cell cycle between parasites in the blood and adipose
319 tissue, we measured the DNA synthesis (S phase) in parasites isolated from both tissues. For that,
320 mice infected for five days with the same monomorphic strain were intravenously injected with 5-
321 ethynyl-2-deoxyuridine (EdU), a thymidine analogue that is actively incorporated into newly
322 synthesized DNA²⁶. After 30 minutes, blood and adipose tissue parasites were isolated from a pool
323 of two mice and analyzed by microscopy *ex vivo* for the percentage of EdU positive cells (Fig. 4C).
324 The ATF population showed on average a lower percentage of labeled cells than BSFs (15.8% vs
325 24.6%, respectively) (Fig. 4D), indicating that the ATF population has fewer cells entering DNA
326 synthesis. In parallel, we performed an *ex vivo* EdU labeling of parasites previously isolated from
327 a pool of two mice infected for the same period with the same strain. EdU labeling *ex vivo*
328 corroborated our observations *in vivo*, indicating that the parasite isolation protocol does not affect
329 DNA synthesis (Supplementary Fig. S2B). The profile of KsNs together with the EdU incorporation
330 analysis, clearly indicate that the cell cycle of parasites in the fat and blood is different. ATFs appear
331 to spend more time in G1 than their blood counterparts.

332 Finally, we determined the doubling time of parasites in blood and adipose tissue. For that,
333 mice were infected with monomorphic parasites previously labelled *in vitro* with CellTrace™ Violet
334 (CTV), a fluorescent dye that binds to all free amines inside cells. Every time a cell divides, the
335 amount of CTV is halved²⁷, which allows the estimation of doubling time by scoring the fluorescence
336 intensity in labeled parasites (see Experimental Procedures). 2 days post-infection, we performed
337 intravital microscopy of the blood and adipose tissue populations (Fig. 4E) and we measured the
338 intensity of the CTV-positive cells. The adipose tissue revealed a more heterogeneous population
339 with mean fluorescence intensities oscillating between 3.7 and 489.3, whereas the bloodstream
340 forms mean fluorescence intensity oscillated between 0.1 and 72.6 (Fig. 4F). Indeed, 40% of the
341 studied adipose tissue population displayed exclusive high intensities of CTV. The calculated
342 doubling time of BSFs was 6.2 hours, which is in good agreement with previous reports for both *in*
343 *vivo* and *in vitro* growth of BSFs^{28,29}. In contrast, the doubling time of ATFs was 12.4 hours, i.e.
344 twice longer than BSFs (Fig. 4G). To exclude that the staining background detected *in vivo* was
345 influencing our analysis, we also did the analysis *ex vivo*, in two isolated labeled populations. The
346 *ex vivo* data clearly corroborated the intravital microscopy observations: BSFs presented a doubling
347 time of 6.2 hours contrasting to ATFs 11.6 hours (Supplementary Fig. S2C).

348
349 Overall, our results show that in the adipose tissue, the slender form parasites have a
350 reduced protein synthesis and a concomitantly reduced growth rate. Together with our initially
351 reported observation that ATFs are metabolically distinct from bloodstream counterparts, we
352 conclude that colonization of adipose tissue triggers a persistent behavior in *T. brucei*.

353

354

355 Discussion

356

357 The occurrence of non-dividing or slow growing cells in persistent infections is well
358 documented for bacteria and has gained attention in parasitic protozoa in the last 10-15 years.
359 Here, we show that, relative to their blood counterparts, the slender forms residing in the adipose
360 tissue (ATFs) divide more slowly and synthesize less proteins, two hallmarks of persistence. This
361 existence of persister-like cells in *T. brucei* infections may be important for disease chronicity and
362 could contribute to treatment failure.

363

364 Dynamic infection modeling predicts slow growing parasites

365 Our model analysis adds an extra layer of complexity to the published models, typically
366 focused on antigenic variation or differentiation mechanisms^{10,13,16,30}. Here we addressed the
367 existence of differences between parasite dynamics in different in-host compartments, namely the
368 blood and adipose tissue, anticipating an adipose tissue population that replicates 2-fold more
369 slowly than the blood population, which is consistent with the temporal and magnitude trends
370 present in the data.

371 Besides testing for inter-compartmental variability, this modeling approach also provides
372 estimates for other relevant parameters involved in infection, such as the migration rate between

373 compartments and contribution to clearance by the immune response. Model 2, for instance,
374 predicts a migration rate of about 0.11 cells/mg/day suggesting that, per milligram of organ, each
375 day about 11% of blood parasites leave to the adipose tissue and vice-versa (0.005 per hour). This
376 observation is in line with previously estimated migration rates between blood and organs of mice
377 infected with *Salmonella enterica* (0.005 per hour)³¹. Similarly, the lower bound for the ratio
378 between slender vs stumpy cells killing rates, estimated by the joint posterior of this model in the
379 interval 6.5-24, also falls within the reported estimated range 5-7³², although we find more
380 uncertainty with this dataset. The remaining parameter estimates are similar between models and
381 approximate existing values in the literature (e.g. antigen switching rate)^{13,30}.

382 Naturally, the space for modeling is infinite, but including additional complexity is a
383 stepwise process, ideally backed by different and incremental sources of data. Having found
384 support for one major difference between the two compartments, does not rule out the existence
385 of other sources of variation that may, on their own, or synergistically, contribute to further
386 individuation of infection dynamics between the blood and adipose tissue. Future models, based
387 on more-detailed infection time-series data (e.g. explicit antigenic variants, more time points for
388 parasite densities, tissue-specific immune responses), combined with proteomics and high-
389 resolution microscopy, should be developed. This would allow assess to other dimensions of blood
390 and adipose tissue variations, and integrate them in frameworks for parasite fitness in natural
391 transmission settings³³. Expanding the description of variant-specific traits or time-dependent
392 phenotypes, such as gradual immune suppression, could help capture more accurately the
393 intricacies of peak-to-peak variability that the current modeling framework does not account for. It
394 would also be interesting to characterize other extravascular populations, by modelling other
395 relevant and inter-linked in-host compartments such as the brain and the skin, and quantify their
396 thus far-unexplored role in chronic infection.

397 398 **Cell-cycle remodeling and metabolic switch**

399 Persisters are defined as slow-growing or growth-arrested cells, with a metabolism adapted
400 to the available nutrients and their energetic demands². This phenotype may arise stochastically or
401 in response to environmental cues such as nutrient limitation. When nutrient resources are not
402 optimal, some bacteria remodel their metabolism and reduce their growth and protein synthesis, to
403 become persisters. Persisters have been described in bacterial populations including
404 *Mycobacterium*, *Streptococcus*, *Staphylococcus* and *Candida*³⁴. Reports on protozoan parasites
405 are more recent and less detailed but vast enough to accommodate different species like *T. cruzi*,
406 *Leishmania spp.*, *Plasmodium spp.* and *T. gondii*². Adapting to the mammalian host
407 microenvironments by acquiring persistence is a common strategy between parasites.

408 Inside the mammalian host, *T. brucei* colonizes several organs, including the adipose
409 tissue, pancreas, skin and brain^{5,9}. The proteomic analysis showed metabolic changes in ATFs
410 resembling the ones observed in persistent parasitic protozoa, suggesting that the adipose tissue
411 population could harbor persistent parasites. First, and foremost, the protein synthesis machinery
412 is downregulated, while the pathway that produces ATP and acetate from pyruvate is upregulated.
413 The observed increase of the purine salvage pathway in ATFs may reflect a need to increase the
414 ATP production capacity in the adipose tissue environment. Interestingly, ATFs appears to share
415 some features with stumpy forms, while it also shows important differences. Like stumpy forms,
416 ATFs appear to show an increased production of ATP, via the acetate pathway³⁵ and an
417 upregulation of the enzymes of the glutamine/proline degradation pathway^{36,37}. Unlike stumpy
418 forms, ATFs did not show evidence for upregulation of the Protein Associated with Differentiation
419 1 (PAD1), a major hallmark of stumpy forms. The characteristic upregulations of Expression Site
420 Associated Gene 9 (ESAG9), Protein Phosphatase 1 (PP1) and RNA-binding Protein 7 (RBP7) in
421 stumpy forms were also not observed in the ATFs proteome³⁸.

422 Another evidence that supports that ATFs may be persister cells is that the division time of
423 ATFs is twice longer than BSFs. Reduced cell growth is the first evidence for the presence of
424 persister cells in a population, consistent among bacterial and protozoan persisters². Recently,
425 Ward et al. reported the existence of *T. cruzi* persistent slow grower cells in the colon of chronically
426 infected mice³⁹. Also, *T. gondii*, one of the most widespread protozoan parasites, owes its
427 persistent infection nature to metabolically active, transient slow grower persistent bradyzoites
428 inhabiting tissue cysts as a strategy to face nutrient limitations and host immune pressure³.

429 In *T. brucei* life cycle, two stages consist of parasites in which cell cycle has been arrested:
430 the stumpy and metacyclic forms. Exit from cell cycle arrest only takes place when those parasites

431 have been transmitted to the new hosts, the Tsetse and the mammal, respectively^{6,7}. In ATFs, we
432 did not find evidence for a complete cell cycle arrest but rather a reduced growth. Moreover, in
433 contrast to stumpy and metacyclic forms, ATFs can recolonize a new microenvironment within the
434 mammalian host⁸, indicating that the persistent behavior of ATFs is reversible within the
435 mammalian host.

436

437 The extended presence of *T. brucei* parasites in the adipose tissue suggests that this
438 reservoir might play a role in infection. Parasite evasion by migration to extravascular spaces
439 together with persister-like phenotype may be a strategic protection from the immune response²,
440 allowing for periodical blood repopulation. Alternatively, the reduced growth might be a
441 consequence of a metabolic adaptation to the tissue environment, which could ultimately be
442 associated to the wasting syndrome characteristic of trypanosomiasis in humans and cattle⁴⁰. In
443 the future, it would be interesting to test the metabolic and replicative behavior of parasites that
444 colonize other tissues and test whether the persistence-behavior is specific to the adipose tissue.

445 Similar to what has been proposed for dormant *T. gondii* and persistent *L. donovani* cells,
446 among other parasitic protozoa², the proteome of *T. brucei* adipose tissue parasites also showed
447 upregulation of proteins involved in oxidative stress and downregulation of proteins involved in
448 protein synthesis. Intriguingly, the latter has been pointed as one of the explanations for drug
449 resistance in persistent cells^{2,41}. It is tempting to speculate that *T. brucei* adipose tissue forms may
450 be more resistant to drugs and contribute to relapses. Drug resistance has been a major concern
451 in African Trypanosomiasis treatment given the observed relapses in treated patients^{42,43}. The
452 reasons for these observations are still a matter of debate in the literature. Our observation of
453 persistent-like cells among the adipose tissue population of parasites (and possibly in other
454 colonized tissues as well) could contribute to explain treatment failure, just as it does so in other
455 persistent bacteria and parasitic infections. Novel efficient strategies for drug therapies must be
456 based on, and incorporate improved knowledge of these persistent cell populations, especially their
457 mechanisms, as a way to overcome their refractoriness and promote sterile cure.

458

459

460 **Methods**

461

462 **Parasite Cell Lines**

463 To characterize the infection dynamics, a *T. brucei* pleomorphic stumpy reporter cell line
464 was used (AnTat1.1 *GFP::PAD1_{utr}*) while for the remaining experiments, a monomorphic strain was
465 selected (Lister 427), to avoid the mixture of the two life cycle stages (slender and stumpy forms).
466 Procytic forms (PCFs) were obtained from Lister 427 cultured parasites, by placing 2 million
467 parasites in 1mL of DTM medium with 6mM of cis-aconitic acid at 27°C with 5% CO₂ and allowing
468 them to grow for 3 days.

469

470 **Animal Infections and Parasites Isolation**

471 Animal experiments were performed according to EU regulations and approved by the
472 Órgão Responsável pelo Bem-estar Animal (ORBEA) of Instituto de Medicina Molecular and the
473 competent authority Direção Geral de Alimentação e Veterinária (license number: 018889 \2016).
474 Mice were group-housed in filter-top cages in a Specific-Pathogen-Free barrier facility under
475 standard laboratory conditions: 21 to 22°C and a 12 h light/12 h dark cycle. Chow and water were
476 available ad libitum. All infections were performed in 8-11 week old wild-type male C57BL/6J mice
477 with origin in Charles River, France, by intraperitoneal (i.p.) injection of 2000 parasites, unless
478 otherwise stated. Parasite viability was evaluated prior to infection under an optical microscope.

479 Parasites were collected from mice sacrificed by CO₂ narcosis. Blood parasites were
480 collected first by heart puncture, while adipose tissue parasites collection was performed on
481 perfused gonadal depots incubated in HMI11 (or Creek's Minimal Medium, for the proteomics
482 assay) at 37°C for up to 70 minutes. Mice were manually transcidentally perfused with pre-warmed
483 heparinized saline buffer (50mL 1X phosphate buffered saline (1X PBS) with 250µL of 5000 I.U./mL
484 heparine per animal). Subsequently, parasites were isolated using a DEAE sepharose TM Fast
485 Flow column whenever necessary (GE Healthcare).

486

487 **Infection Dynamics**

488 Parasitemia was assessed daily by taking blood from the mouse-tail vein and counting the
489 number of parasites using a Neubauer chamber. The total number of parasites present in the blood
490 and the gonadal depot was determined by qPCR. Briefly, animals were sacrificed by CO₂ narcosis
491 and blood collected by heart puncture. Blood sample was split into two. On one sample, red blood
492 cells were lysed with Red Blood Cell Lysis Buffer (0.15M ammonium chloride; 0.01M potassium
493 bicarbonate; 0.001M EDTA disodium salt) and the remaining pellet snap frozen in liquid nitrogen.
494 The other sample was used for parasites isolation. After perfusion, gonadal depots were collected
495 and one was snap frozen immediately while the other was used to isolate fat parasites. Genomic
496 DNA (gDNA) was extracted from tissues using NZY tissue gDNA isolation kit (NZYTech, Portugal)
497 and the amount of 18S rDNA gene of *T. brucei* present in the blood and the gonadal depots was
498 measured by qPCR and converted into number of parasites as described in⁸. Isolated parasites
499 from blood and gonadal adipose tissue were then fixed and their GFP expression was analyzed on
500 a BD LSRFortessa™ cell analyzer and data treated using FlowJo.

501

502 **Mathematical Modeling**

503 Average parasite densities and percentage of stumpy forms obtained from both blood and
504 adipose tissue gonadal depot during the infection dynamics characterization were used to fit the
505 mathematical model. The ordinary differential equations for population dynamics were based on¹³,
506 but in this study the number of compartments was doubled to represent parasites growing in the
507 blood and adipose tissue, and the immune response dynamics was simplified. The model variables
508 for each antigenic wave were the slender and stumpy cells in the two compartments, as well as the
509 variant-specific immune response. Allowing for up to five consecutive antigenic waves during 28
510 days resulted in 25 inter-dependent equations. Thus, infection processes were captured with a
511 parsimonious formulation (growth, density-dependent differentiation, antigenic variation and
512 antigen-dependent host immune response). Further, the two in-host compartments, blood and
513 adipose tissue, were connected through migration, assumed to occur at the same rate in either
514 direction and for all cells. All variants were assumed symmetric, in their parameters, including the
515 switch rate to the next wave. The majority of parameters were estimated by fitting the model to the
516 dynamic data; with exception of a few such as, the stumpy cell lifespan which was fixed at about 2
517 days¹³ (Supplementary Model Information for detailed description on model structure and biological
518 assumptions).

519 Model fitting to data was performed under a Bayesian framework, using the adaptive Monte
520 Carlo Markov chain mcmcstat package in Matlab⁴⁴. To compare hypotheses, Deviance Information
521 Criterion (DIC)¹⁴, the posterior error distribution and marginal likelihood¹⁵ were computed for each
522 model, and the quality of fits to data and feasibility of parameters were inspected.

523

524 **Proteomics**

525 Mice infected for 5 days were sacrificed and parasite isolation from blood and adipose
526 tissue was performed as described above. Parasites were washed in Creeks Minimal Medium
527 depleted from Fetal Bovine Serum and lysed with 1X LDS Buffer supplemented with 100mM
528 Dithiothreitol (DTT) by boiling at 80°C for 15 minutes. Parasites isolated from up to 6 mice were
529 pooled to obtain a minimum of 0.32 million parasites. Protein samples were then separated,
530 prepared and measured as in⁴⁵ except for the peptide elution. This step was performed with a 200
531 minutes optimized gradient from 2 to 40% acetonitrile with 0.1% formic acid at a flow rate of
532 225nL/min. Protein quantification was processed in MaxQuant version 1.6.7.0⁴⁶ using standard
533 settings. The raw proteomics files were searched against the protein databases of *T. brucei*
534 TREU927 (TriTrypDB version 33), *Mus musculus* strain C57BL/6J (UniProt), the 14 VSGs of the
535 Lister 427 *T. brucei* strain (UniProt) and the contaminants database included in MaxQuant.
536 Contaminants, reverse Protein Groups (PGs) and PGs only identified by a modification site or by
537 less than 2 peptides (of which 1 needed to be unique) were removed as well as *M. musculus*
538 identified proteins. To assign a quantification to missing values, these were imputed 1000 times
539 using a β -distribution with equal shape parameters ($\alpha=\beta=2$) and a PG was only considered
540 differentially regulated if it was found up or downregulated in at least 99% of times. For each
541 individual replicate, the obtained distribution was scaled between 0.1 and 1.5 percentile of the log₂
542 transformed measured label-free quantitation (LFQ) intensity values. Finally, only the PGs that
543 were quantified by LFQ intensity in at least 2 replicates of one condition (ATFs or BSFs) were
544 considered for further analysis. Regulated PGs were determined if the relationship between the

545 significance of the Welch's t-test and their fold-change was above a threshold defined by a
546 reciprocal function (with limits p-value=0.05 and fold change=1.5).

547 The GO term enrichment analysis was performed in R with GO.db annotation package⁴⁷
548 from Bioconductor and Fisher's Exact Test (p-value ≤ 0.05) from stats package. *T. brucei* TREU927
549 GO term annotations were obtained from TriTrypDB and GO term enrichment was assessed. PGs
550 were associated with the GO terms of the individual genes in the group and a GO term enrichment
551 test was performed separately on upregulated and downregulated gene. Only the GO terms with
552 at least 5 annotated PGs were considered.

553 The mass spectrometry proteomics data have been deposited to the ProteomeXchange
554 Consortium via the PRIDE partner repository with the dataset identifier PXD014958.

555

556 **Protein Synthesis**

557 Differences in protein synthesis were determined through Click-iT[®] Homopropargylglycine
558 (HPG) incorporation into nascent proteins. To establish the ideal concentration of HPG, cultured
559 Lister 427 parasites were washed in methionine free Minimal Essential Medium and incubated in
560 the same medium with 25µM, 50µM or 100µM of HPG for 30 minutes at 37°C. Cultured parasites
561 were also incubated in the same medium with 100µg/mL of cycloheximide for 20 minutes at 37°C
562 before adding 50µM HPG. Isolated BSFs and ATFs as well as PCFs were also incubated with
563 50µM HPG under the same conditions. After incubation, all tested parasites were fixed with 1%
564 paraformaldehyde and permeabilized with 0.5% Triton X-100. 100µL of the reaction cocktail were
565 then added for a 30-minute period at room temperature (light protected) and samples washed after
566 with 100µL of Reaction Rinse Buffer (Click-iT[®] HPG Alexa Fluor[®] 488 Protein Synthesis Assay Kit).
567 All samples were stained with 1µg/mL of DAPI and both DAPI and HPG intensities measured with
568 BD LSRFortessa X-20. Data analyses were performed in FlowJo. Statistical significances were
569 determined by Wilcoxon signed-rank test in the free software R: <http://www.r-project.org>.

570

571 **Cell-cycle Profile**

572 The number of kinetoplasts and nuclei were assessed for both blood and adipose tissue
573 populations by microscopy imaging *in vivo* and *ex vivo*. To compare the two profiles, parasites from
574 a pool of 2 mice infected for 5 days were stained either by intravenous injection of 10mg/kg of
575 Hoechst H33342 (*in vivo* experiments) or by adding 1µg/mL of Hoechst H33342 (*ex vivo*
576 experiments) and observed by intravital microscopy and *ex vivo* microscopy, respectively. More
577 than 600 cells were analyzed per condition.

578

579 **DNA synthesis**

580 Measurement of DNA synthesis was based on the incorporation of 5-ethynyl-2'-
581 deoxyuridine (EdU) and its subsequent detection by a fluorescent azide through "click" chemistry.
582 EdU was either administered intravenously (200mg/kg) to mice infected for 5 days (*in vivo* protocol),
583 or added (100µM) to parasites isolated from mice infected for the same period and cultured in
584 HMI11 at 37°C (*ex vivo* protocol). In both conditions, parasites were incubated with EdU for 30
585 minutes. The remaining protocol was conducted mostly according to manufacturer's instructions
586 with some minor changes (ThermoFisher Scientific). Briefly, parasites were washed with cold
587 1xTDB, fixed with 1% paraformaldehyde for 10 minutes followed by quenching with 0.125M glycine
588 for 5 minutes. Parasites were adhered to silanized coverslips for 30 minutes, permeabilized with
589 0.5% Triton X-100 for 20 minutes, washed twice with 3%BSA in 1xPBS and fluorescently labeled
590 with Alexa Fluor[®] 488 fluorescent azyde by exposure to 300µL of Click-iT[®] reaction cocktail for an
591 extra 30 minutes, protected from light. Finally, cells were washed twice with 3%BSA in 1xPBS,
592 stained with 1µg/mL of Hoechst H33342 for 30 minutes and the percentage of EdU positive cells
593 was assessed by fluorescence microscopy. All the reported steps were performed at room
594 temperature. More than 300 cells were analyzed per condition.

595

596 **Cell Proliferation**

597 10 million cultured parasites were labelled with 2µM of CellTrace[™] Violet in 10mL 1xPBS
598 for 20 minutes at 37°C, protected from light. Remnants of free dye were removed by adding 5mL
599 of HMI11 to the cells for 5 minutes at 37°C. Pelleted parasites were then resuspended in HMI11
600 and 1 million immediately intraperitoneally injected in a mouse. A fraction of these parasites was
601 fixed with 1% paraformaldehyde for 10 minutes followed by quenching with 0.125M glycine for 5
602 minutes and pellet resuspended in 3%BSA/0.05% TX-100 in 1xPBS and observed by microscopy

603 to determine basal die incorporation. Two days post-infection, the Mean Fluorescence Intensity
604 (MFI) levels of CTV within blood and adipose tissue parasites were assessed either by intravital
605 microscopy or by *ex vivo* microscopy analyses. More than 180 cells were analyzed per condition.
606 The doubling time was estimated by obtaining the number of divisions of each population (x) from
607 the slope of the CTV intensity versus the number of divisions ($y=C_0e^{-0.693x}$, where y is the
608 determined mean fluorescence intensity of the analyzed population and C₀ is initial mean
609 fluorescence intensity of the population used to infect mice) and then dividing the infection time by
610 the obtained number of divisions (x).

611
612

613 **Microscopy**

614 All imaging was performed on a 3i Marianas spinning disc confocal microscope (Intelligent
615 Imaging Innovations) using a 63× objective lens (Plan-Apochromat, NA 1.40, oil immersion, Zeiss).
616 Laser stacks 405 (405nm) and 488 (488nm) were used for visualizing kinetoplasts and nuclei
617 (Hoechst) or CTV, and FITC-Dextran, respectively. To avoid photodamage, an average maximum
618 laser power of 2mW, a gain value of 1 and an exposure of 100 milliseconds were selected. A time
619 lapse of 5 seconds was acquired, with images obtained every 10 milliseconds. In addition, bright
620 field imaging was performed for visualization of infected parasites in the blood monolayer and BSFs
621 and ATFs *ex vivo*. Background correction was performed with internal controls (i.e. regions without
622 parasites in CTV positive samples for CTV experiments and cytoplasmic regions of parasites for
623 EdU experiments) and exogenous controls (i.e. parasites in CTV- or EdU-negative samples).
624 Segmentation (CTV experiments) was based on the bright field (blood) or 488nm (adipose tissue
625 and blood) detections, and mean fluorescence intensity (MFI) was calculated for each parasite
626 based on the CTV signal (405nm), Hoechst H33342 signal (405nm), or Click-iT™-EdU signal
627 (488nm). Parasites were imaged across the full available sample using a “snake by rows”
628 observation and acquisition approach covering the entire tissue/dish. For all tested conditions, a
629 minimum of 50 parasites per sample was imaged in a minimum of 25 different fields of view.
630 Acquired images were then analyzed in Fiji⁴⁸ and Ilastik (<https://www.ilastik.org>).

631
632

632 **Sample Preparation for Microscopy**

633 Prior to intravital microscopy, mice were anaesthetized with 120mg/Kg ketamine and
634 16mg/Kg xylazine injected intravenously. FITC-Dextran 70kDa was also injected intravenously
635 immediately preceding imaging to distinguish between blood vessels and tissue parenchyma. The
636 gonadal adipose tissue was exposed through a small incision of 20-40mm made on the lower
637 abdominal region of the mouse and a temporal glass window (Merck rectangular coverglass,
638 100mm x 50mm) implanted for imaging. The mouse was then placed on the microscope stage, and
639 the infected blood vessels from the adipose tissue and the adipose tissue *per se*, were imaged to
640 assess a sample of the BSFs and ATFs population, respectively. This protocol was applied to both
641 gonads. BSFs population was also assessed by imaging blood monolayers obtained from 2μL of
642 collected blood, diluted in 200μL of 1xPBS and placed on a petri dish. Non-motile parasites were
643 excluded from the analysis.

644 For *ex vivo* microscopy, isolated ATFs and BSFs were concentrated into 200μl by
645 centrifugation for 2 minutes at 10,000rcf. The 200μl were then transferred to a glass bottom dish
646 (Matek Life Sciences, 60mm, No. 1.5 thickness) and imaged.

647
648

649 **Acknowledgments**

650

651 The authors thank Keith Matthews (University of Edinburgh) for providing AnTat1.1E clone,
652 Christian Janzen (University of Wurzburg) for the *GFP::PAD1_{utr}* cell line, Ruy M. Ribeiro for useful
653 discussions about the statistical analysis and Helena Pinheiro for drawing the diagram of the
654 mathematical infection model. The authors would like to acknowledge the Rodents, Bioimaging and
655 Flow Citometry Units of the Instituto de Medicina Molecular and all members of the L.M.F. lab. This
656 work was supported by IC&DT Programa de Actividades Conjuntas – ref. 016417 “Oneida”, 771714
657 (ERC) and 029161 (FCT), SFRH/BPD/89833/2012 (FCT) to S.T, LT000047/2019-L (HFSP) and
658 ALTF 1048-2016 (EMBO) to M.D.N, IMM/BI/83-2017 (FCT individual fellowship, project number
659 PTDC/BIM-MET/4471/2014) to T.B.R, IMM/BI/54-2016 (FCT individual fellowship, project number
660 PTDC/BIM-MET/4471/2014)to F.BE and CEECIND/03322/2108 (FCT) to L.M.F.

661

662 **Author Contributions**

663

664 S.T, M.D.N, J.F, E.G, L.M.F designed research; S.T, M.D.N, M.C.Q, T.B.R, F.BE, F.BU, E.G
665 performed experiments; S.T, M.D.N, M.C.S, M.D, F.BR, E.G, L.M.F analyzed data and S.T, F.BR,
666 E.G, L.M.F wrote the paper.

667

668 **Competing Interests**

669

670 The authors declare no competing interests.

671

672 **References**

673

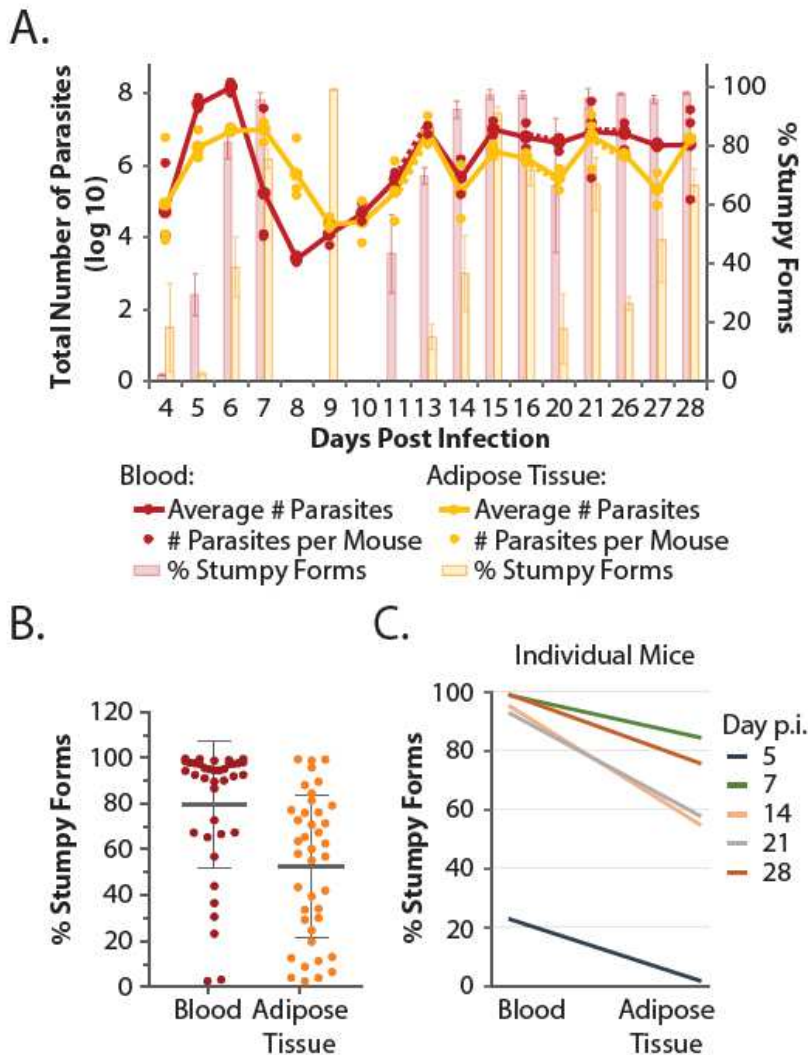
- 674 1. Fisher, R. A., Gollan, B. & Helaine, S. Persistent bacterial infections and persister cells. *Nat.*
675 *Rev. Microbiol.* **15**, 453–464 (2017).
- 676 2. Barrett, M. P., Kyle, D. E., Sibley, L. D., Radke, J. B. & Tarleton, R. L. Protozoan persister-like
677 cells and drug treatment failure. *Nat. Rev. Microbiol.* **17**, 607–620 (2019).
- 678 3. Watts, E. *et al.* Novel approaches reveal that toxoplasma gondii bradyzoites within tissue
679 cysts are dynamic and replicating entities in vivo. *mBio* **6**, 1–24 (2015).
- 680 4. Chen, N. *et al.* Fatty acid synthesis and pyruvate metabolism pathways remain active in
681 dihydroartemisinin-induced dormant ring stages of plasmodium falciparum. *Antimicrob.*
682 *Agents Chemother.* **58**, 4773–4781 (2014).
- 683 5. Pereira, S. S., Trindade, S., De Niz, M. & Figueiredo, L. M. Tissue tropism in parasitic
684 diseases. *Open Biol.* **9**, (2019).
- 685 6. Rico, E. *et al.* Bloodstream form pre-adaptation to the tsetse fly in Trypanosoma brucei.
686 *Front. Cell. Infect. Microbiol.* **4**, 1–15 (2013).
- 687 7. Christiano, R. *et al.* The proteome and transcriptome of the infectious metacyclic form of
688 Trypanosoma brucei define quiescent cells primed for mammalian invasion. *Mol. Microbiol.*
689 **106**, 74–92 (2017).
- 690 8. Trindade, S. *et al.* Trypanosoma brucei Parasites Occupy and Functionally Adapt to the
691 Adipose Tissue in Mice. *Cell Host Microbe* **19**, 837–48 (2016).

- 692 9. Niz, M. De, Bras, D., Pedro, M. & Nascimento, A. M. Organotypic endothelial adhesion
693 molecules are key for *Trypanosoma brucei* tropism and virulence. (2021).
- 694 10. MacGregor, P., Savill, N. J., Hall, D. & Matthews, K. R. Transmission stages dominate
695 trypanosome within-host dynamics during chronic infections. *Cell Host Microbe* **9**, 310–8
696 (2011).
- 697 11. Vanwalleghem, G., Morias, Y., Beschin, A., Szymkowski, D. E. & Pays, E. *Trypanosoma brucei*
698 growth control by TNF in mammalian host is independent of the soluble form of the
699 cytokine. *Sci. Rep.* **7**, 1–7 (2017).
- 700 12. MacGregor, P., Szöör, B., Savill, N. J. & Matthews, K. R. Trypanosomal immune evasion,
701 chronicity and transmission: an elegant balancing act. *Nat. Rev. Microbiol.* **10**, 431 (2012).
- 702 13. Gjini, E., Haydon, D. T., Barry, J. D. & Cobbold, C. A. Critical interplay between parasite
703 differentiation, host immunity, and antigenic variation in trypanosome infections. *Am. Nat.*
704 **176**, 424–439 (2010).
- 705 14. Spiegelhalter, D. J., Best, N. G., Carlin, B. P. & Van Der Linde, A. Bayesian measures of model
706 complexity and fit. *J. R. Stat. Soc. Ser. B Stat. Methodol.* **64**, 583–616 (2002).
- 707 15. Wilks, S. S. The Large-Sample Distribution of the Likelihood Ratio for Testing Composite
708 Hypotheses. *Ann. Math. Stat.* **9**, 60–62 (1938).
- 709 16. Tyler, K. M., Higgs, P. G., Matthews, K. R. & Gull, K. Limitation of *Trypanosoma brucei*
710 parasitaemia results from density-dependent parasite differentiation and parasite killing by
711 the host immune response. *Proc. R. Soc. B Biol. Sci.* **268**, 2235–2243 (2001).
- 712 17. Dejung, M. *et al.* Quantitative Proteomics Uncovers Novel Factors Involved in
713 Developmental Differentiation of *Trypanosoma brucei*. *PLOS Pathog.* **12**, e1005439 (2016).
- 714 18. Van Hellemond, J. J., Opperdoes, F. R. & Tielens, A. G. M. Trypanosomatidae produce
715 acetate via a mitochondrial acetate:succinate CoA transferase. *Proc. Natl. Acad. Sci. U. S. A.*
716 **95**, 3036–3041 (1998).

- 717 19. Mazet, M. *et al.* Revisiting the Central Metabolism of the Bloodstream Forms of
718 *Trypanosoma brucei*: Production of Acetate in the Mitochondrion Is Essential for Parasite
719 Viability. *PLoS Negl. Trop. Dis.* **7**, 1–14 (2013).
- 720 20. Mochizuki, K. *et al.* The ASCT/SCS cycle fuels mitochondrial ATP and acetate production in
721 *Trypanosoma brucei*. *Biochim. Biophys. Acta - Bioenerg.* **1861**, 148283 (2020).
- 722 21. Johnston, K. *et al.* Mapping the metabolism of five amino acids in bloodstream form
723 *Trypanosoma brucei* using U-13C-labelled substrates and LC–MS. *Biosci. Rep.* **39**, 1–17
724 (2019).
- 725 22. Capewell, P. *et al.* Regulation of *Trypanosoma brucei* Total and Polysomal mRNA during
726 Development within Its Mammalian Host. *PLoS ONE* **8**, (2013).
- 727 23. Zhang, M., Joyce, B. R., Sullivan, W. J. & Nussenzweig, V. Translational control in
728 *Plasmodium* and *Toxoplasma* parasites. *Eukaryot. Cell* **12**, 161–167 (2013).
- 729 24. Martin, J. L. *et al.* Metabolic Reprogramming during Purine Stress in the Protozoan Pathogen
730 *Leishmania donovani*. *PLoS Pathog.* **10**, (2014).
- 731 25. T. Sherwin and K. Gull. The cell division cycle of *Trypanosoma brucei brucei* timing of event
732 markers and cytoskeletal modulations. *Philos Trans R Soc Lond B Biol Sci* **323**, 573–88
733 (1989).
- 734 26. Simeonov, A. A chemical method for fast and sensitive detection of DNA synthesis in vivo:
735 Commentary. *Assay Drug Dev. Technol.* **6**, 157–158 (2008).
- 736 27. Lyons, A. B. & Parish, C. R. Determination of lymphocyte division by flow cytometry. *J.*
737 *Immunol. Methods* **171**, 131–137 (1994).
- 738 28. Haanstra, J. R. *et al.* Proliferating bloodstream-form *Trypanosoma brucei* use a negligible
739 part of consumed glucose for anabolic processes. *Int. J. Parasitol.* **42**, 667–673 (2012).
- 740 29. Peacock, L., Ferris, V., Bailey, M. & Gibson, W. Fly transmission and mating of *Trypanosoma*
741 *brucei brucei* strain 427. *Mol. Biochem. Parasitol.* **160**, 100–106 (2008).

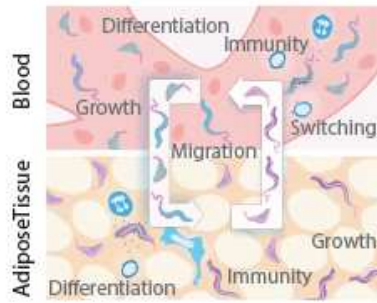
- 742 30. Lythgoe, K. A., Morrison, L. J., Read, A. F. & Barry, J. D. Parasite-intrinsic factors can explain
743 ordered progression of trypanosome antigenic variation. *Proc. Natl. Acad. Sci. U. S. A.* **104**,
744 8095–100 (2007).
- 745 31. Grant, A. J. *et al.* Modelling within-host spatiotemporal dynamics of invasive bacterial
746 disease. *PLoS Biol.* **6**, 757–770 (2008).
- 747 32. McLintock, L. M. L., Turner, C. M. R. & Vickerman, K. Comparison of the effects of immune
748 killing mechanisms on *Trypanosoma brucei* parasites of slender and stumpy morphology.
749 *Parasite Immunol.* **15**, 475–480 (1993).
- 750 33. Gjini, E., Haydon, D. T., Barry, J. D. & Cobbold, C. A. Linking the antigen archive structure to
751 pathogen fitness in African trypanosomes. *Proc. R. Soc. B Biol. Sci.* **280**, (2013).
- 752 34. van den Bergh, B., Fauvart, M. & Michiels, J. Formation, physiology, ecology, evolution and
753 clinical importance of bacterial persisters. *FEMS Microbiol. Rev.* **41**, 219–251 (2017).
- 754 35. Van Grinsven, K. W. A., Van Den Abbeele, J., Van Den Bossche, P., Van Hellemond, J. J. &
755 Tielens, A. G. M. Adaptations in the glucose metabolism of procyclic *Trypanosoma brucei*
756 isolates from tsetse flies and during differentiation of bloodstream forms. *Eukaryot. Cell* **8**,
757 1307–1311 (2009).
- 758 36. Naguleswaran, A., Doiron, N. & Roditi, I. RNA-Seq analysis validates the use of culture-
759 derived *Trypanosoma brucei* and provides new markers for mammalian and insect life-cycle
760 stages. *BMC Genomics* **19**, 1–11 (2018).
- 761 37. Queiroz, R., Benz, C., Fellenberg, K., Hoheisel, J. D. & Clayton, C. Transcriptome analysis of
762 differentiating trypanosomes reveals the existence of multiple post-transcriptional regulons.
763 *BMC Genomics* **10**, 495 (2009).
- 764 38. Silvester, E., McWilliam, K. R. & Matthews, K. R. The cytological events and molecular
765 control of life cycle development of *Trypanosoma brucei* in the mammalian bloodstream.
766 *Pathogens* **6**, 1–19 (2017).

- 767 39. Ward, A. I., Olmo, F., Atherton, R., Taylor, M. C. & Kelly, J. M. Trypanosoma cruzi
768 amastigotes have a reduced replication rate during chronic stage infections. *bioRxiv* (2020).
- 769 40. WHO. WHO Report on Global Surveillance of Epidemic-prone Infectious Diseases World.
770 (2000).
- 771 41. Pontes, M. H. & Groisman, E. A. A physiological basis for nonheritable antibiotic resistance.
772 *mBio* **11**, 1–13 (2020).
- 773 42. Pépin, J. & Khonde, N. Relapses following treatment of early-stage Trypanosoma brucei
774 gambiense sleeping sickness with a combination of pentamidine and suramin. *Trans. R. Soc.*
775 *Trop. Med. Hyg.* **90**, 183–186 (1996).
- 776 43. Richardson, J. B. *et al.* Whole genome sequencing shows sleeping sickness relapse is due to
777 parasite regrowth and not reinfection. *Evol. Appl.* **9**, 381–393 (2016).
- 778 44. Haario, H., Laine, M., Mira, A. & Saksman, E. DRAM: Efficient adaptive MCMC. *Stat. Comput.*
779 **16**, 339–354 (2006).
- 780 45. Bluhm, A., Casas-Vila, N., Scheibe, M. & Butter, F. Reader interactome of epigenetic histone
781 marks in birds. *Proteomics* **16**, 427–436 (2016).
- 782 46. Cox, J. & Mann, M. MaxQuant enables high peptide identification rates, individualized
783 p.p.b.-range mass accuracies and proteome-wide protein quantification. *Nat. Biotechnol.*
784 **26**, 1367–1372 (2008).
- 785 47. A. Alexa and J. Rahnenfuhrer. Enrichment Analysis for Gene Ontology. topGO R package
786 version 2.24.0. (2016).
- 787 48. Schindelin, J. *et al.* Fiji: An open-source platform for biological-image analysis. *Nat. Methods*
788 **9**, 676–682 (2012).
- 789
790
791

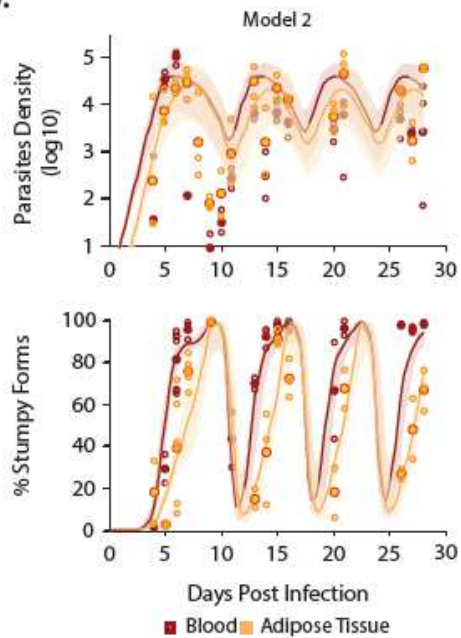


795
 796 **Figure 1. Infection dynamics in blood and gonadal adipose tissue.**
 797 **A.** C57BL/6J mice were infected with a pleomorphic *T. brucei* *GFP::PAD1_{utr}* stumpy reporter cell-
 798 line. The total number of parasites in each tissue was quantified by qPCR (red and yellow lines and
 799 dots) and the percentage of stumpy forms was estimated by FACS as the proportion of GFP-
 800 positive parasites (red and yellow bars). Data for each day of infection was obtained from a pool of
 801 2-9 mice (n=2-4 independent experiments per time point). The dashed lines correspond to
 802 noncontiguous time points and the full lines to contiguous time points. On days 8-11, with two
 803 exceptions, it was not possible to measure the proportion of stumpy forms due to a decrease in
 804 parasite load. **B.** Percentage of stumpy forms in blood (red) and gonadal adipose tissue (yellow)
 805 for the 17 studied time points. Each point represents one independent measurement (either from a
 806 single mouse or from a pool of up to 3 mice). Grey lines represent the average percentage of
 807 stumpy forms and error bars the standard deviation. **C.** Percentage of stumpy forms in blood and
 808 gonadal adipose tissue of five mice sacrificed at different days of infection (5, 7, 14, 21 and 28).
 809

A.

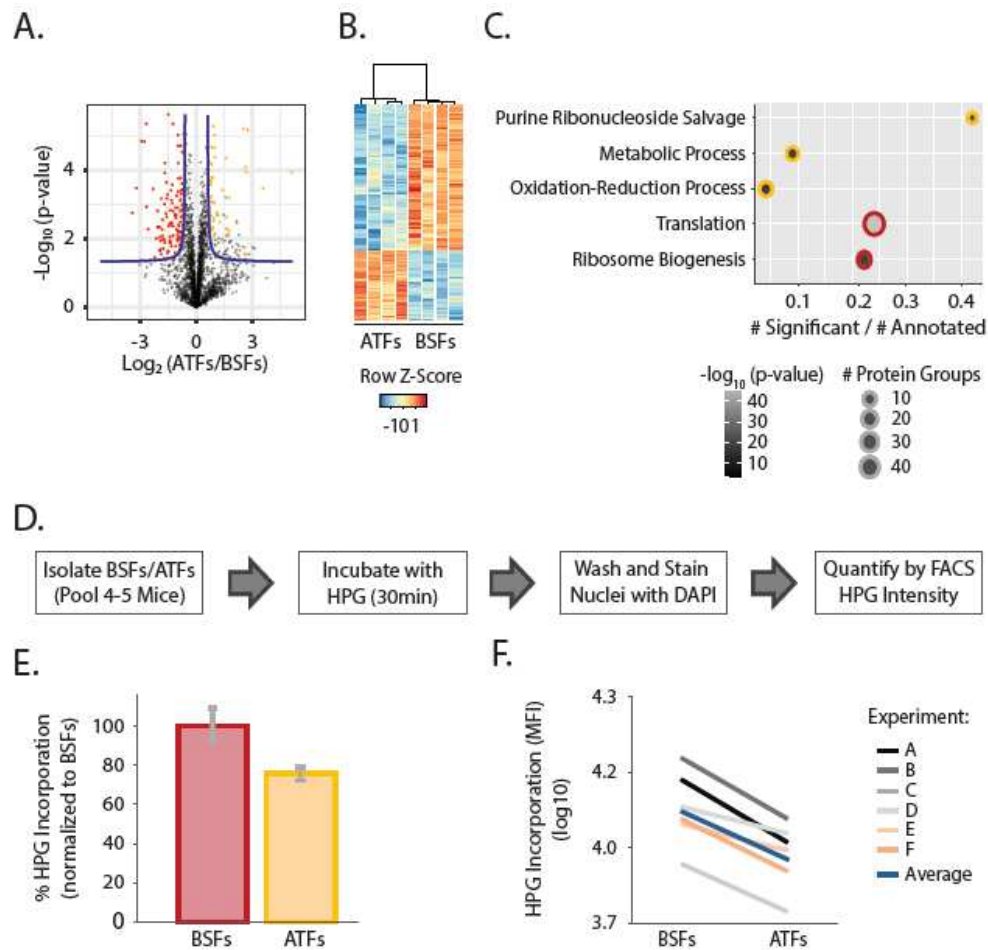


B.



810
811
812
813
814
815
816
817
818
819
820
821
822
823
824
825

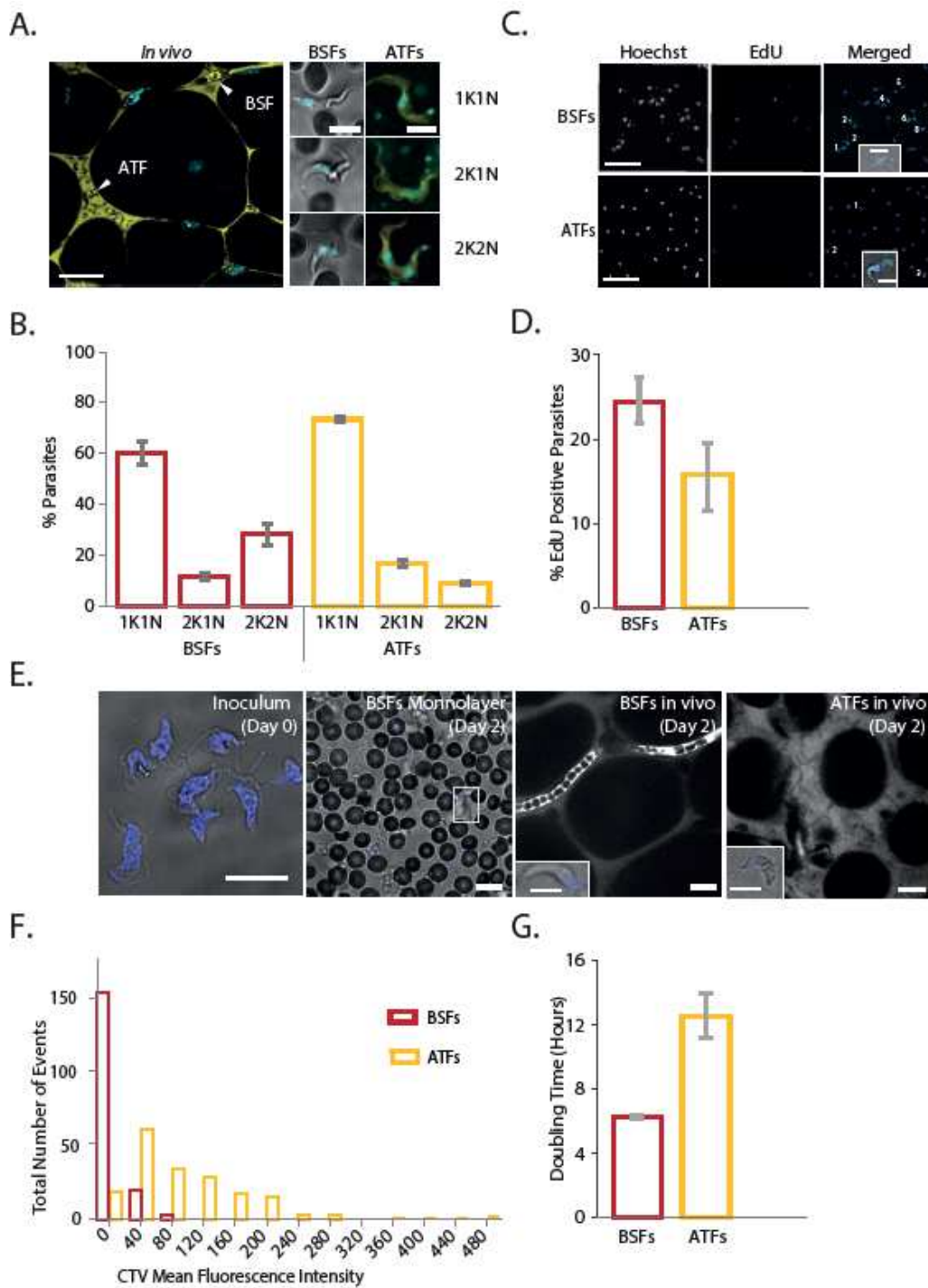
Figure 2. Mathematical model for parasite dynamics in blood and gonadal adipose tissue.
A. Diagram of the mathematical infection model. In this model, two compartments were considered: blood and adipose tissue. In each compartment, parasites may have intrinsic growth and differentiation rates. A constant migration rate was also considered between the two. The specific immune response was assumed to be triggered due to overall antigen stimulation from blood and adipose tissue parasites, after which it grows in response to increasing pathogen density and reaches each compartment (Materials and Methods and Supplementary Model Information). **B.** Model fit for predictions of parasite density and proportion of stumpy forms, in blood and adipose tissue, for the favored model (Model 2). Scattered empty circles indicate all observations from individual time-points and filled circles indicate the mean over replicates used to fit the model. The lines indicate the model prediction with mean parameters (as in Table 1). The shaded regions indicate the 95% credible envelopes from 50 simulations with random parameter combinations from the estimated posteriors.



826
827
828
829
830
831
832
833
834
835
836
837
838
839
840
841
842
843
844
845
846
847
848

Figure 3. Proteome analysis and protein synthesis of parasites isolated from blood and gonadal adipose tissue.

A. Representative volcano plot of 1 out of the 1000 performed imputations with the 2693 protein groups detected by mass spectrometry in the sum of BSFs and ATFs 8 data sets. Red and yellow dots indicate protein groups significantly upregulated in BSFs and ATFs respectively. Proteins were obtained from Lister 427 parasites isolated from a pool of 5-6 animals infected for 5 days ($n=4$ independent experiments). **B.** Heat map representing the z-score abundances of the differentially expressed protein groups. Each column corresponds to one independent pool of mice. **C.** Enriched GO terms (Biological Process) of the differentially upregulated (yellow circles) and downregulated (red circles) proteins according to gene ratio, using a False Discovery Rate corrected p-value cut-off of 0.05 (Fisher's exact test). Each dot corresponds to a given GO term: the size represents the number of differentially expressed protein groups and the color the respective p-value. **D.** Fluxogram of the experimental procedure used to quantify protein synthesis in Lister 427 parasites isolated from blood and gonadal adipose tissue 5 days post-infection. **E.** Percentage of HPG internalized by ATFs (yellow bar) normalized to the percentage of internalization of the BSFs (red bar) ($n=6$ independent experiments). Error bars represent the Standard Error of the Mean. **F.** Mean Fluorescence Intensity of the HPG incorporated for 30 minutes by the isolated BSFs and ATFs for experiments A, B, C, D; E and F and for the average of the six experiments ($n= 6$ independent experiments).



849
850
851
852
853
854
855
856
857
858
859
860

Figure 4. Parasite proliferation in blood and gonadal adipose tissue.

A. Cell-cycle analysis assayed by the number of Kinetoplasts (K) and Nuclei (N) in BSFs and ATFs Lister 427 parasites from mice infected for 5 days (n= 4 independent experiments). Left side: Representative image of *in vivo* microscopy of the adipose tissue and a vessel (scale bar, 20µm); Right side: representative images of the three parasites analyzed on a monolayer (BSFs) and *in vivo* (ATFs) (Hoechst staining, blue; scale bar, 5µm). **B.** Quantification of cell cycle analysis. Percentage of parasites containing 1K1N (cells in G1, early S phase or G0-arrested cells), 2K1N (G2 and mitotic cells) and 2K2N (post-mitotic). More than 800 cells per condition. **C.** DNA synthesis assayed by the incorporation *in vivo* of EdU. *Ex vivo* microscopy images of Lister 427 BSFs and ATFs carrying recently synthesized DNA labelled with EdU (n=5 independent experiments). 5 days

861 post-infection, 200mg/kg of EdU were administered intravenously and, 30 minutes later, mice were
862 sacrificed and the parasites isolated, labeled with Alexa Fluor® 488 in a Click-it reaction, and
863 analyzed by microscopy. In the merged images, the EdU staining is shown by the Alexa Fluor 488
864 (green), which colocalizes with the nucleus and the kinetoplast, both stained with Hoechst (blue)
865 (scale bar, 20µm). Insets: Representative images of labeled parasites (scale bar, 5µm). **D.**
866 Quantification of DNA synthesis assay. Percentage of BSFs and ATFs that incorporated the
867 thymidine analogue (EdU), representing the proportion of parasites that were in S phase or entered
868 S phase during the 30 minutes pulsing period. More than 300 cells per condition. **E.** Doubling-time
869 assayed by CellTrace™ Violet (CTV) staining dynamics. Representative images of *ex vivo*
870 microscopy showing the inoculum of CTV labelled parasites (blue), a monolayer of BSFs stained
871 with CTV (blue) and intravital microscopy of ATFs and BSFs (scale bar, 20µm). Insets:
872 Representative images of labeled parasites (scale bar, 5µm). **F.** Distribution of the CTV Mean
873 Fluorescence Intensity of blood and adipose tissue parasites assessed by intravital microscopy
874 (n=183 BSFs and n=199 ATFs pooled from the 4 independent experiments). **G.** Quantification of
875 CTV assay. Doubling time of BSFs and ATFs from mice infected for 2 days (n=4 independent
876 experiments). Doubling time estimated for BSFs and ATFs considering the decrease in CTV signal
877 intensity during 2 days. Doubling time was assessed by intravital microscopy of BSFs and ATFs
878 from mice infected with cultured Lister 427 parasites pre-labeled with 2µM of CTV for 20 minutes
879 immediately prior to infection. More than 180 cells per condition.
880
881

882
883

Table 1. Mathematical Models Parameters and Estimates

Parameter	Interpretation	Estimates ¹			Units
		Model 1	Model 2	Model 3	
r	Growth Rate	2.12 (7.8*) (1.85 ; 2.40)	-	-	Divisions/Per Day
r_b	Growth Rate of Slender Forms in Blood	-	2.38 (7.0*) (2.10 ; 2.56)	2.33 (7.1*) (2.14 ; 2.49)	Divisions/Per Day
r_f	Growth Rate of Slender Forms in Adipose Tissue	-	1.21 (13.7*) (1.01 ; 1.56)	1.23 (13.5*) (1.01 ; 1.69)	Divisions/Per Day
d	Minimal Killing Rates for Slender Forms ²	0.0016 (0.0001 ; 0.0063)	0.0032 (0.0005 ; 0.0066)	0.0029 (0.0006 ; 0.0065)	Cells/mg/Day
d'	Minimal Killing Rates for Stumpy Forms ²	0.0005 (0.0001 ; 0.0028)	0.0001 (0.00005 ; 0.0008)	0.0002 (0.00005 ; 0.0009)	Cells/mg/Day
K	Density for Maximal Differentiation	12600 (3400 ; 51000)	31300 (6700 ; 58700)	-	Cells/mg
K_b	Density for Maximal Differentiation in Blood	-	-	26400 (4000 ; 58100)	Cells/mg
K_f	Density for Maximal Differentiation in Adipose Tissue	-	-	14200 (3300 ; 54200)	Cells/mg
k	Density for Half-Saturation Immune Stimulation	830 (210 ; 6440)	3600 (990 ; 16600)	3400 (1200 ; 14000)	Cells/mg
σ	Activation Rate of Anti VSG Immune Response	1.38 (1.04 ; 1.83)	1.68 (1.27 ; 2.21)	1.67 (1.28 ; 2.21)	Per Day
μ	Migration Rate Across Compartments	0.0117 (0.0069 ; 0.0311)	0.1075 (0.0523 ; 0.1901)	0.0633 (0.0101 ; 0.8353)	Cells/mg/Day
s	Switch Probability to Next Antigenic Wave in Blood	0.0007 (0.0001 ; 0.0051)	0.0004 (0.0001 ; 0.0014)	0.0006 (0.0002 ; 0.0019)	Per Division

¹ Mean (95% CI)

² Number of killed cells by 1 unit of immune response due to the feedback from VSG-specific immunity

* Doubling time (hours)

884

Supplementary Files

This is a list of supplementary files associated with this preprint. Click to download.

- [TrindadeSupplementaryInformation.pdf](#)
- [TrindadeSupplementaryInformationMovieS1.avi](#)
- [TrindadeSupplementaryInformationDataset.xlsx](#)